

Valley-dependent exciton fine structure and Autler–Townes doublets from Berry phases in monolayer MoSe₂

Chaw-Keong Yong^{1,10*}, M. Iqbal Bakti Utama^{1,2,3,10}, Chin Shen Ong^{1,3}, Ting Cao^{1,3}, Emma C. Regan^{1,3,4}, Jason Horng⁵, Yuxia Shen⁶, Hui Cai⁷, Kenji Watanabe⁸, Takashi Taniguchi⁸, Sefaattin Tongay⁶, Hui Deng⁵, Alex Zettl^{1,3,9}, Steven G. Louie^{1,3} and Feng Wang^{1,3,9*}

The Berry phase of Bloch states can have profound effects on electron dynamics^{1–3} and lead to novel transport phenomena, such as the anomalous Hall effect and the valley Hall effect^{4–6}. Recently, it was predicted that the Berry phase effect can also modify the exciton states in transition metal dichalcogenide monolayers, and lift the energy degeneracy of exciton states with opposite angular momentum through an effective valley-orbital coupling^{7–11}. Here, we report the observation and control of the Berry phase-induced splitting of the 2p exciton states in monolayer molybdenum diselenide (MoSe₂) using the intraexciton optical Stark spectroscopy. We observe the time-reversal-symmetric analogue of the orbital Zeeman effect resulting from the valley-dependent Berry phase, which leads to energy difference of +14 (–14) meV between the 2p₊ and 2p_– exciton states in the K (K') valley, consistent with the ordering from our ab initio GW-Bethe–Salpeter equation results. In addition, we show that the light–matter coupling between intraexciton states is remarkably strong, leading to a prominent valley-dependent Autler–Townes doublet under resonant driving. Our study opens up pathways to coherently manipulate the quantum states and excitonic excitation with infrared radiation in two-dimensional semiconductors.

In the momentum space of atomically thin transition metal dichalcogenides (TMDs), a pair of degenerate exciton states are present at the K and K' valleys, producing a valley degree of freedom that is analogous to the electron spin^{12–14}. The electrons in the K and K' valleys acquire a finite Berry phase when they traverse in a loop around the band extrema, with the phase equal in magnitude but opposite in sign at the K and K' valleys, as required by the time-reversal symmetry^{1,12–14}. The Berry phase not only has close connections to the optical selection rules that allow optical generation and detection of the valley-polarized carriers by circularly polarized photons^{12–17} but also plays a central role in novel electron dynamics and transport phenomena in TMD and graphene layers, such as the valley Hall effect^{4–6,13,18}.

In principle, the Berry phase, together with other effects from inversion symmetry breaking, can have profound consequences

for the wavefunction and energy spectrum of the excited states in two-dimensional (2D) materials. TMD monolayers are known to host strongly bound excitons with a remarkably large exciton binding energy due to enhanced Coulomb interactions in two dimensions^{19–23}, and lead to the observation of intraexcitonic transition at mid-infrared frequency^{21–23}. It was recently predicted that the Berry curvature of Bloch states can add an anomalous term to the group velocity of electrons and holes and creates an energy splitting between exciton states with opposite angular momentum^{1,3,7–10}, as illustrated in Fig. 1a. Figure 1b shows a simplified exciton energy spectrum illustrating the exciton fine structure based on our ab initio GW-Bethe–Salpeter equation (GW-BSE) calculations. The 2p₊ and 2p_– exciton states are split in energy with opposite order for the K and K' valleys due to the opposite chirality in the two valleys^{7–9,13}. Such novel exciton fine structure, which embodies important wavefunction properties arising from the Bloch band geometry, can strongly modify the intraexcitonic light–matter interactions. Experimental observation of this predicted exciton spectrum, however, has been challenging, because it requires a new spectroscopic probe that can distinguish both the momentum valley and the exciton angular momentum.

Here, we report the observation of the Berry phase effect in the exciton energy spectrum of monolayer MoSe₂ using intraexciton optical Stark spectroscopy. We demonstrate that the degeneracy between the 2p_± exciton states is lifted by the Berry phase effect, enabling a valley-dependent Autler–Townes doublet from strong intraexciton light–matter coupling. We coherently drive the intraexciton transitions using circularly polarized infrared radiation, which couples the 1s exciton to the 2p₊ or 2p_– states selectively through the pump photon polarization (solid arrowed lines in Fig. 1b). The pump-induced changes in the 1s exciton transition are detected by circularly polarized probes, which selectively measure the K or K' valley excitons. Independent control of pump and probe photon polarization enables us to distinguish the exciton fine structures in the K and K' valleys. We determine an energy splitting of 14 meV between the 2p₊ and 2p_– exciton states within a single valley, and this energy splitting changes sign between the K and K' valleys.

¹Department of Physics, University of California at Berkeley, Berkeley, CA, USA. ²Department of Materials Science and Engineering, University of California at Berkeley, Berkeley, CA, USA. ³Materials Sciences Division, Lawrence Berkeley National Laboratory, Berkeley, CA, USA. ⁴Graduate Group in Applied Science and Technology, University of California at Berkeley, Berkeley, CA, USA. ⁵Department of Physics, University of Michigan, Ann Arbor, MI, USA. ⁶School for Engineering of Matter, Transport and Energy, Arizona State University, Tempe, AZ, USA. ⁷Center for Nanophase Materials Sciences, Oak Ridge National Laboratory, Oak Ridge, TN, USA. ⁸National Institute for Materials Science, Tsukuba, Japan. ⁹Kavli Energy NanoScience Institute at University of California Berkeley, Berkeley, CA, USA. ¹⁰These authors contributed equally: Chaw-Keong Yong, M. Iqbal Bakti Utama. *e-mail: chawkeong@berkeley.edu; fengwang76@berkeley.edu

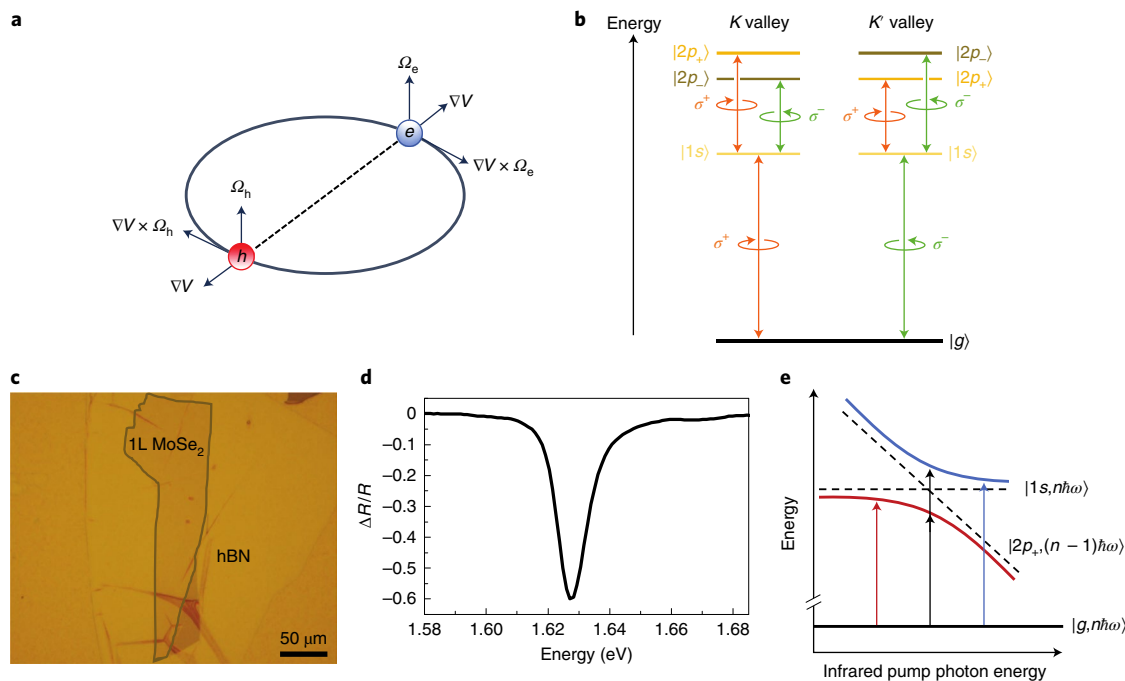


Fig. 1 | Schematics of exciton spectrum and optical transition in monolayer MoSe₂. **a**, Diagram illustrating the effects of Berry curvature Ω_e and Ω_h on the energy of exciton. The electron and hole acquire an anomalous velocity $\nabla V \times \Omega$ in a central potential $V(r)$, resulting in a lift of the degeneracy between the exciton states with opposite angular momentum. **b**, Illustration of the optical transition and selection rules for one-photon and two-photon excitations in the K and K' valleys of monolayer MoSe₂. $|g\rangle$, $|1s\rangle$, $|2p_- \rangle$ and $|2p_+ \rangle$ denote the ground state, $1s$, $2p_-$ and $2p_+$ exciton states, respectively. The symbols σ^+ and σ^- denote left- and right-circular polarization states, respectively. **c**, Optical micrograph of monolayer (1L) MoSe₂ encapsulated by hBN layers on alumina-coated silver substrate. **d**, The reflection contrast of hBN-encapsulated monolayer MoSe₂ on an alumina-coated silver surface at 77 K. It shows prominent A-exciton resonance at 1.627 eV with a full-width at half-maximum of ~9 meV. **e**, Schematic illustrating the avoided-crossing behaviour due to quantum-mechanical coupling between the infrared photons field and the $1s$ - $2p_+$ electronic transition. The dashed lines show the energy difference between the $|g, n\hbar\omega\rangle$ and the unperturbed $|1s, n\hbar\omega\rangle$ and $|2p_+, (n-1)\hbar\omega\rangle$ states as a function of the infrared pump photon energy. The blue and red solid lines show the dressed exciton states from quantum hybridization. The arrows show the optical transitions from the ground state to the dressed $1s$ exciton state.

We determine the $1s$ - $2p$ transition dipole moment to be 55 ± 6 D. This leads to an optical Stark shift that is almost 40 times larger than that in the interband counterpart^{24–26} under the same pump detuning and driving optical field strength. Such strong and valley-dependent intraexciton transitions open-up new pathways for the coherent manipulation of quantum states in 2D semiconducting materials using infrared radiation.

To investigate the fine structure of the excitonic p -manifold, we fabricated a high-quality MoSe₂ monolayer that is encapsulated in hexagonal boron nitride (hBN) layers using mechanical exfoliation and stacking following ref.²⁴. The sandwiched hBN/MoSe₂/hBN heterostructure was then transferred to an alumina-coated silver surface (Fig. 1c). The device was kept in vacuum at 77 K for all optical measurements. Figure 1d shows the reflection contrast spectrum of the MoSe₂ monolayer, which exhibits a prominent A-exciton absorption feature at energy $E_{1s} = 1.627$ eV with a full-width at half-maximum of 9 meV. This A-exciton peak arises from the optical transition between the ground state and the lowest energy $1s$ exciton state in the MoSe₂ monolayer, which is well-separated from the higher-lying exciton states due to strong Coulomb interactions in TMD monolayers^{10,11,21,27}.

We used intraexciton optical Stark spectroscopy with helicity-defined pump and probe light to selectively access the $2p_+$ or $2p_-$ exciton states in the K and K' valleys. As illustrated in Fig. 1b, we drive the $1s$ - $2p_+$ intraexciton transition coherently with a σ^+ -polarized infrared pump and monitor the photoinduced changes in the $1s$ exciton absorption at K and K' valleys with σ^+ and σ^- optical probes, respectively (where σ^+ and σ^- denote left-handed and right-handed circular polarization, respectively). Quantum-mechanical

coupling between the infrared photon field and the $1s$ - $2p_+$ electronic transition leads to an avoided-crossing behaviour that modifies the $1s$ exciton state systematically with the changing infrared photon energy, as illustrated in Fig. 1e. Specifically, the $|1s, n\hbar\omega\rangle$ and $|2p_+, (n-1)\hbar\omega\rangle$ states hybridize when driven by the infrared pump in the 'dressed atom' picture, where n is the integer number of infrared pump photons at frequency ω and \hbar is Planck's constant/ 2π . When the infrared photon energy is below (above) the $1s$ - $2p_+$ resonance, the non-resonant hybridization leads to a decreased (increased) energy for the $1s$ exciton state. When the infrared photons are resonant with the $1s$ - $2p_+$ transition, perfect hybridization between the $|1s, n\hbar\omega\rangle$ and $|2p_+, (n-1)\hbar\omega\rangle$ states leads to an energy splitting in the $1s$ exciton absorption. The pump-induced optical Stark shift and splitting of the $1s$ exciton in the K and K' valleys can be detected from the $1s$ exciton absorption spectrum by using σ^+ - and σ^- -polarized probe light, respectively. This allows us to explicitly identify the $1s$ - $2p_+$ intraexciton transition in each valley. Since the infrared pump photon energy is much lower than the transition energy of the $1s$ exciton, our measurement scheme probes only the coherent optical Stark effects without non-coherent contribution from real carrier generation.

Figure 2a–c shows the transient reflection signals for the σ^+ -polarized probe, which measures the photoinduced changes of the K-valley exciton transition on excitation with a σ^+ infrared pump of different energies (E_p). The driving pump has an effective driving intensity (I_{eff}) of 7 ± 1 MW cm⁻², which corresponds to a local optical field strength (E_{eff}) of 70 ± 10 kV cm⁻¹ (see Supplementary information). The colours in Fig. 2a–c represent the pump-induced change of the probe reflectivity ΔR , which is directly proportional

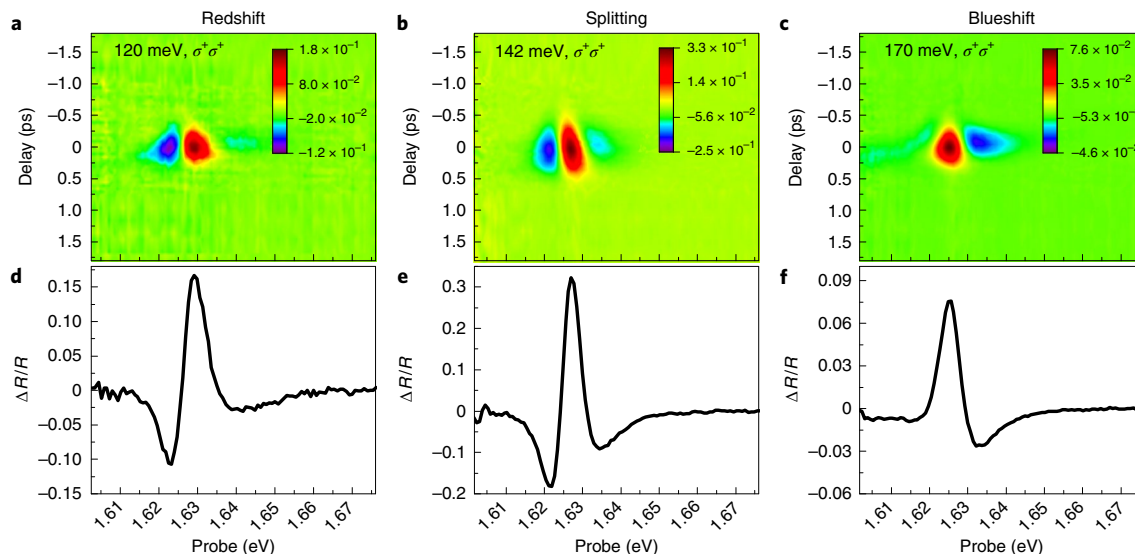


Fig. 2 | Transient reflection spectra of K-valley exciton transitions. **a–c**, Two-dimensional plot of transient reflection spectra of the K-valley 1s exciton resonance of MoSe₂ at 77 K following photoexcitation with σ^+ -polarized infrared pump at photon energy of 120 meV (**a**), 142 meV (**b**) and 170 meV (**c**). The colour scale, vertical axis and horizontal axis represent the relative reflectivity change $\Delta R/R$, the pump-probe time delay τ and the probe photon energy, respectively. Positive (negative) $\Delta R/R$ represents a decrease (increase) of absorption. The photoinduced absorption in the K valley 1s exciton is monitored by σ^+ -polarized probes. The signals are finite only when the pump and probe pulses overlap in time, indicating an instantaneous coherent response and negligible excitation of real exciton population. **d–f**, At $\tau = 0$ ps, the coherent signals for σ^+ -probes exhibit spectral responses that are characteristic of energy redshift (**d**) to splitting (**e**) and then to energy blueshift (**f**) as the driving photon energy is increased from 120 meV to 170 meV.

to the change of absorption. The positive (negative) ΔR , is proportional to the decrease (increase) of absorption. The horizontal and vertical axes show the probe energy and pump-probe time delay τ , respectively. Strong transient signals are present for pump-probe delays close to zero and they become negligible at pump-probe delays larger than 500 fs. These instantaneous signals confirm the optical responses arise from coherent optical Stark effects. By changing the driving energy of the σ^+ pump, the optical response varies significantly. Figure 2d–f displays the corresponding transient spectra of the K-valley exciton at $\tau = 0$ ps. At $E_p = 120$ meV, the absorption of the K-valley exciton exhibits a decrease above E_{1s} and an increase below E_{1s} , corresponding to a redshift of the 1s exciton resonance due to the optical Stark effect. The photoinduced response is opposite for $E_p = 170$ meV, which is dominated by transition energy blueshift. The spectrum at $E_p = 142$ meV, in contrast, shows an increase of absorption at energies both above and below E_{1s} and a reduction of absorption at E_{1s} , which is consistent with an energy splitting of the 1s exciton peak.

The evolution of the 1s exciton absorption in monolayer MoSe₂ under coherent infrared driving can be better visualized directly from the optical absorption spectra characterized by the imaginary part of optical susceptibility (χ_{im}) (see Supplementary information)²⁸. Figure 3a shows the absorption spectra of the 1s exciton at $\tau = 0$ ps for both the K and K' valleys driven by σ^+ -polarized infrared radiation of different photon energies. It shows clearly that the 1s exciton transition exhibits avoided-crossing behaviour in both valleys, which evolves gradually from energy blueshift to splitting and then to redshift as the pump photon energy is decreased. However, there is an important distinction between the K and K' valley spectra: the resonant coupling between the σ^+ -infrared photons and the $1s-2p_+$ intraexciton transition, which splits the 1s exciton resonance, occurs at driving photon energy of 142 meV and 128 meV in the K and K' valleys, respectively. It shows that the $1s-2p_+$ intraexciton transition energy differs by 14 meV for the K and K' valleys. Due to the time-reversal symmetry between K and K' valleys in monolayer MoSe₂, this observation also indicates that the $2p_+$ and $2p_-$ exciton

states are non-degenerate and have an energy difference of 14 meV in a single valley (Fig. 1b).

We further plot the blue- and redshifted 1s resonance as a function of the infrared pump photon energy in Fig. 3c. We find that the energy shifts induced by the intraexciton optical Stark effect are almost 40 times larger than its interband counterpart at the same pump intensity and resonance detuning^{24–26}.

Since the driving photon energy is close to the $1s-2p_+$ transition and strongly off-resonant from the interband transition, our observation can be qualitatively understood using a model describing a driven three-state system as illustrated in Fig. 1b,e. Under σ^+ -pump radiation, $|1s, n\hbar\omega\rangle$ hybridizes with $|2p_+, (n-1)\hbar\omega\rangle$, which can be described by the effective Hamiltonian (H_{eff})

$$H_{eff} = \begin{pmatrix} E_{1s} + i\gamma_{1s} & \frac{V_1}{2} \\ \frac{V_1}{2} & E_{1s} + |E_{1s-2p_+}| - E_p + i\gamma_{2p_+} \end{pmatrix} \quad (1)$$

Here V_1 is proportional to the $1s-2p_+$ intraexciton transition dipole moment μ_{1s-2p_+} via $V_1 = \mu_{1s-2p_+} E_{eff}$, where E_{eff} is the local optical field strength on the sample. E_p , E_{1s} and E_{1s-2p_+} denote the pump photon energy, the 1s exciton energy and the $1s-2p_+$ intraexciton transition energy, respectively. γ_{1s} and γ_{2p_+} are the half-width at half-maximum of the 1s and $2p_+$ exciton modes, respectively. Direct diagonalization of the effective Hamiltonian yields two new eigenstates $|\alpha\rangle$ and $|\beta\rangle$, which are energetically separated by $V' = \sqrt{V_1^2 + (\Delta + i\gamma_{2p_+} - i\gamma_{1s})^2}$, where $\Delta \equiv E_p - |E_{1s-2p_+}|$ is the detuning energy. The optical absorption of the probe photon to the new eigenstates can then be computed (see Supplementary information).

Figure 3b shows the calculated absorption spectra at different driving energies. The E_{1s-2p_+} used in the fitting is 142 meV and 128 meV for K and K' valleys, respectively. From the fitting to the experimental data, we extracted an exciton-photon coupling constant V_1 of 8 meV, which corresponds to a $1s-2p_+$ intraexciton transition dipole moment μ_{1s-2p_+} of 55 ± 6 D. The μ_{1s-2p_+} is almost 6 times larger than that effective dipole moment in the interband exciton

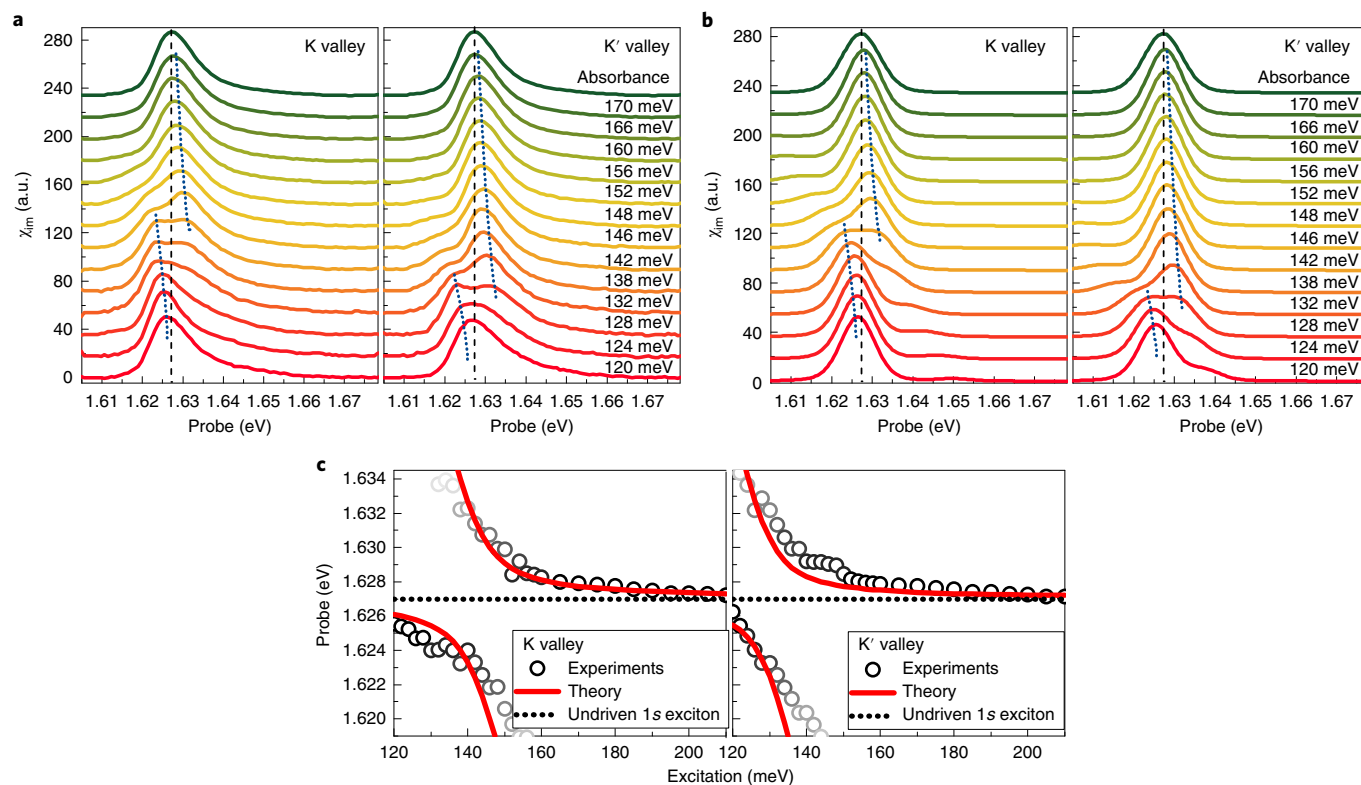


Fig. 3 | Valley-dependent intraexciton optical Stark effect. a, b, Experimentally observed (a) and calculated (b) photoinduced absorption spectra of MoSe₂ monolayer at $\tau = 0$ ps under various σ^+ -pump excitation energies for the K and K' valleys. The dashed lines indicate the peak position of the unperturbed A exciton. The dotted lines are guides to the eyes for the peak position at different driving energies. The spectra are offset for clarity and labelled according to the excitation energy. The spectra evolve from energy redshift to splitting and then to blueshift, as the driving energy is increased. The calculation is based on the Hamiltonian shown in equation (1). Exciton-photon coupling leads to avoided-crossing and the observed peak splitting at resonant coupling. This resonant coupling occurs at driving photon energy of 142 meV and 128 meV in the K and K' valleys, respectively. It corresponds to a Berry phase-induced $1s-2p_+$ intraexciton transition energy difference of 14 meV. **c.** Measured $1s$ exciton peak position (circles) in the K and K' valleys as a function of σ^+ -infrared pump photon energy for an effective driving intensity is 7 ± 1 MW cm⁻². The greyscale shows the relative strength of optical transition. The solid lines show the calculated dressed exciton states based on the Hamiltonian shown in equation (1).

optical Stark effect^{24–26}, and it leads to a nearly 40 times larger optical Stark shift under the same driving intensity and detuning.

To better understand the experimental results, we performed ab initio GW-BSE calculations using the BerkeleyGW^{29–31} package to determine the exciton energy levels and optical selection rules of exciton and intraexciton transitions in monolayer MoSe₂. In these calculations, environmental screening effects from the hBN encapsulation layers are included¹⁹ from first principles (see Supplementary information). The simulation confirms the energy level diagram of the $1s$, $2p_+$ and $2p_-$ excitons and the optical selection rules in K and K' valleys in Fig. 1b. Our calculations find that the energies of the $1s$ and $2p_-$ exciton states are separated by 117 meV, with $2p_+$ exciton states further separated by 7 meV in the K valley. The energetic order of the $2p_+$ and $2p_-$ excitons states is opposite in the K' valley, as a result of time-reversal symmetry. Although the $2p_+$ excitons are dark in linear optics, they are optically active when coupled to the $1s$ exciton with circularly polarized light (Fig. 1b). For example, our calculations show that the $1s-2p_+$ intraexciton transition couples exclusively to the σ^+ light with a transition dipole moment of 42 D. The $1s-2p_-$ intraexciton transition, in contrast, couples exclusively to the σ^- light. The experimentally observed intraexciton dipole moment and valley-dependent exciton fine structure match reasonably well with the ab initio GW-BSE calculations.

The combination of $2p_+$ exciton splitting and extremely strong intraexcitonic light-matter interaction allow us to observe

valley-dependent Autler–Townes doublets in monolayer MoSe₂ at higher pump intensity. Towards this goal, we fabricated a hBN-encapsulated MoSe₂ heterostructure on a zinc sulfide (ZnS) substrate, where the local field factor on the sample for the infrared pump light is more favourable than that for MoSe₂ on an alumina-coated silver substrate (Supplementary information). In this device, the $1s-2p_+$ intraexciton transition energies for the K and K' valleys are determined to be 150 meV and 138 meV, respectively (see Supplementary information). Figure 4a shows the absorption spectra of the $1s$ exciton at $\tau = 0$ ps for the K and K' valleys under series of excitation intensities. The σ^+ -pump driving energy is set to 150 meV, which is on resonance with the $1s-2p_+$ transition in the K valley but positively detuned from the $1s-2p_+$ transition in the K' valley. We observe contrasting coherent phenomena between the K and K' valleys: the $1s$ exciton transition exhibits a striking splitting into the Autler–Townes doublet in the K valley, but shows a mostly blueshift in the K' valley. In contrast, when the σ^+ -pump energy is tuned to 138 meV, which is negatively detuned from the $1s-2p_+$ transition in the K valley but on resonance with the $1s-2p_+$ transition in the K' valley, the $1s$ exciton transition shows redshift in the K valley but a clear Autler–Townes doublet in the K' valley (Fig. 4b). Figure 4c,d shows the splitting energy in the Autler–Townes doublet at resonant excitation scales linearly with the excitation field strength, as expected from equation (1)^{32,33}. At an effective driving intensity of 50 ± 10 MW cm⁻², which corresponds to a local optical

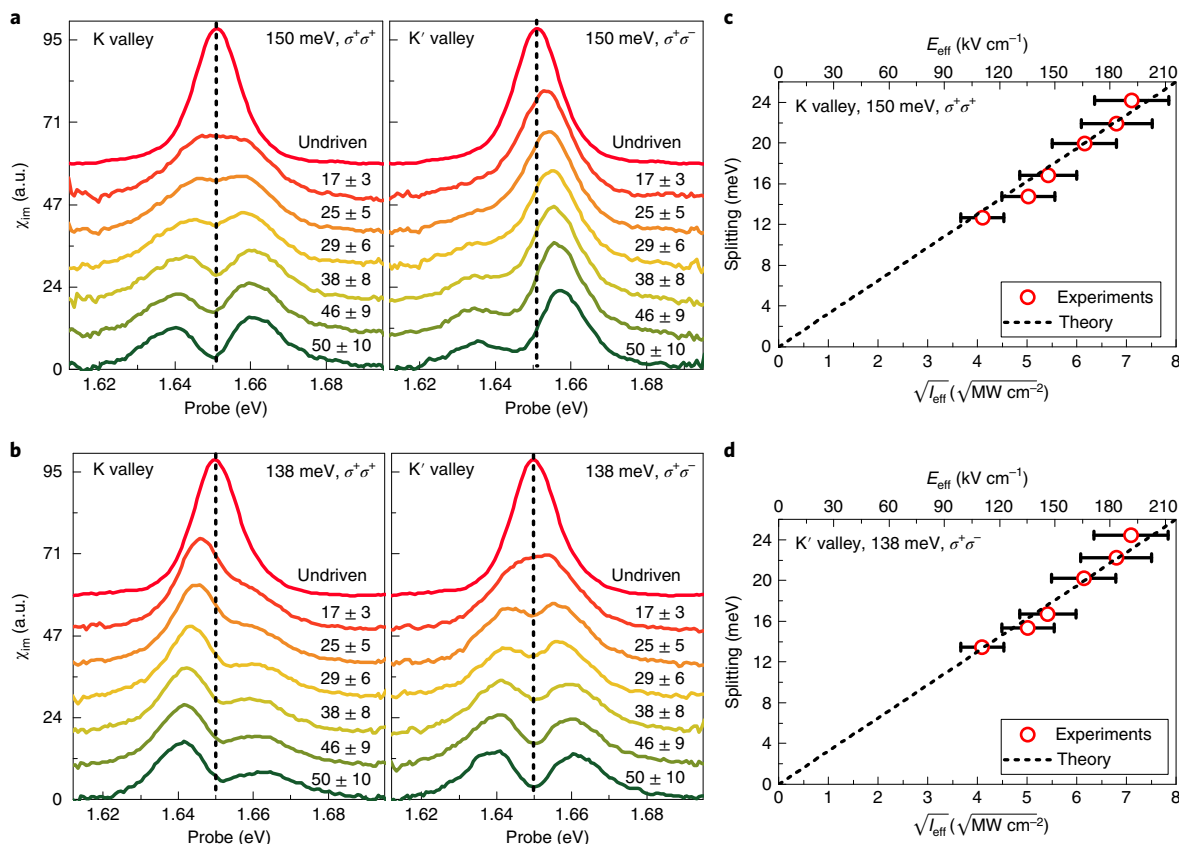


Fig. 4 | Valley-dependent Autler-Townes splitting. **a,b**, Photoinduced absorption spectra of monolayer MoSe₂ on ZnS substrate at $\tau = 0$ ps for a series of σ^+ -pump intensities at a driving energy of 150 meV (**a**) and 138 meV (**b**) for the K and K' valleys. The dashed lines indicate the peak position of the undriven A exciton. The spectra are offset and labelled according to the effective driving intensity (MW cm^{-2}). **c,d**, The dependence of Autler-Townes splitting energy in the K and K' valleys on the squared root of effective pump intensity ($\sqrt{I_{eff}}$) for a driving photon energy of 150 meV (**c**) and 138 meV (**d**), respectively. The top axis shows the corresponding effective local optical field strength (E_{eff}). The splitting energies are obtained from fitting the photoinduced absorption lines with two Lorentzian lines. The dashed lines are fitting obtained from the Hamiltonian shown in equation (1). The error bars correspond to the uncertainties of infrared pump intensity.

field strength of $200 \pm 20 \text{ kV cm}^{-1}$, the Autler-Townes splitting can reach $\sim 24 \text{ meV}$ in both valleys. This Autler-Townes doublet leads to a valley-dependent electromagnetically induced transparency in the $1s$ exciton transition, where the absorption at the $1s$ exciton resonance is reduced by more than tenfold compared with the undriven exciton (Fig. 4a,b). Our findings offer an effective pathway to coherently manipulate the quantum states and excitonic excitations using infrared radiation coupled to the $1s-2p_+$ intraexciton transition.

Online content

Any methods, additional references, Nature Research reporting summaries, source data, statements of code and data availability and associated accession codes are available at <https://doi.org/10.1038/s41563-019-0447-8>.

Received: 23 December 2018; Accepted: 25 June 2019;
Published online: 05 August 2019

References

- Xiao, D., Chang, M.-C. & Niu, Q. Berry phase effects on electronic properties. *Rev. Mod. Phys.* **82**, 1959–2007 (2010).
- Price, H. M., Ozawa, T. & Carusotto, I. Quantum mechanics with a momentum-space artificial magnetic field. *Phys. Rev. Lett.* **113**, 190403 (2014).
- Chang, M.-C. & Niu, Q. Berry phase, hyperorbits, and the Hofstadter spectrum. *Phys. Rev. Lett.* **75**, 1348–1351 (1995).
- Zhang, Y., Tan, Y.-W., Stormer, H. L. & Kim, P. Experimental observation of the quantum Hall effect and Berry's phase in graphene. *Nature* **438**, 201–204 (2005).
- Novoselov, K. S. et al. Unconventional quantum Hall effect and Berry's phase of 2π in bilayer graphene. *Nat. Phys.* **2**, 177–180 (2006).
- Mak, K. F., McGill, K. L., Park, J. & McEuen, P. L. The valley Hall effect in MoS₂ transistors. *Science* **344**, 1489–1492 (2014).
- Zhou, J., Shan, W.-Y., Yao, W. & Xiao, D. Berry phase modification to the energy spectrum of excitons. *Phys. Rev. Lett.* **115**, 166803 (2015).
- Srivastava, A. & Imamoglu, A. Signatures of Bloch-band geometry on excitons: nonhydrogenic spectra in transition-metal dichalcogenides. *Phys. Rev. Lett.* **115**, 166802 (2015).
- Trushin, M., Goerbig, M. O. & Belzig, W. Model prediction of self-rotating excitons in two-dimensional transition-metal dichalcogenides. *Phys. Rev. Lett.* **120**, 187401 (2018).
- Berkelbach, T. C., Hybertsen, M. S. & Reichman, D. R. Bright and dark singlet excitons via linear and two-photon spectroscopy in monolayer transition-metal dichalcogenides. *Phys. Rev. B* **92**, 085413 (2015).
- Wu, F., Qu, F. & MacDonald, A. H. Exciton band structure of monolayer MoS₂. *Phys. Rev. B* **91**, 075310 (2015).
- Xu, X., Yao, W., Xiao, D. & Heinz, T. F. Spin and pseudospins in layered transition metal dichalcogenides. *Nat. Phys.* **10**, 343–350 (2014).
- Xiao, D., Liu, G.-B., Feng, W., Xu, X. & Yao, W. Coupled spin and valley physics in monolayers of MoS₂ and other group-VI dichalcogenides. *Phys. Rev. Lett.* **108**, 196802 (2012).
- Cao, T. et al. Valley-selective circular dichroism of monolayer molybdenum disulphide. *Nat. Commun.* **3**, 887–891 (2012).
- Ye, Z., Sun, D. & Heinz, T. F. Optical manipulation of valley pseudospin. *Nat. Phys.* **13**, 26–29 (2017).

16. Mak, K. F., He, K., Shan, J. & Heinz, T. F. Control of valley polarization in monolayer MoS₂ by optical helicity. *Nat. Nanotechnol.* **7**, 494–498 (2012).
17. Zeng, H., Dai, J., Yao, W., Xiao, D. & Cui, X. Valley polarization in MoS₂ monolayers by optical pumping. *Nat. Nanotechnol.* **7**, 490–493 (2012).
18. Xiao, D., Yao, W. & Niu, Q. Valley-contrasting physics in graphene: magnetic moment and topological transport. *Phys. Rev. Lett.* **99**, 236809 (2007).
19. Ugeda, M. M. et al. Giant bandgap renormalization and excitonic effects in a monolayer transition metal dichalcogenide semiconductor. *Nat. Mater.* **13**, 1091–1095 (2014).
20. Chernikov, A. et al. Exciton binding energy and nonhydrogenic Rydberg series in monolayer WS₂. *Phys. Rev. Lett.* **113**, 076802 (2014).
21. Ye, Z. et al. Probing excitonic dark states in single-layer tungsten disulphide. *Nature* **513**, 214–218 (2014).
22. Poellmann, C. et al. Resonant internal quantum transitions and femtosecond radiative decay of excitons in monolayer WSe₂. *Nat. Mater.* **14**, 889–893 (2015).
23. Merkl, P. et al. Ultrafast transition between exciton phases in van der Waals heterostructures. *Nat. Mater.* **18**, 691–696 (2019).
24. Yong, C.-K. et al. Biexcitonic optical Stark effects in monolayer molybdenum diselenide. *Nat. Phys.* **14**, 1092–1096 (2018).
25. Kim, J. et al. Ultrafast generation of pseudo-magnetic field for valley excitons in WSe₂ monolayers. *Science* **346**, 1205–1208 (2014).
26. Sie, E. J. et al. Valley-selective optical Stark effect in monolayer WS₂. *Nat. Mater.* **14**, 290–294 (2015).
27. Wang, G. et al. Giant enhancement of the optical second-harmonic emission of WSe₂ monolayers by laser excitation at exciton resonances. *Phys. Rev. Lett.* **114**, 097403 (2015).
28. Li, Y. et al. Measurement of the optical dielectric function of monolayer transition-metal dichalcogenides: MoS₂, MoSe₂, WS₂, and WSe₂. *Phys. Rev. B* **90**, 205422 (2014).
29. Deslippe, J. et al. BerkeleyGW: a massively parallel computer package for the calculation of the quasiparticle and optical properties of materials and nanostructures. *Comput. Phys. Commun.* **183**, 1269–1289 (2012).
30. Rohlfing, M. & Louie, S. Electron-hole excitations and optical spectra from first principles. *Phys. Rev. B* **62**, 4927–4944 (2000).
31. Hybertsen, M. & Louie, S. Electron correlation in semiconductors and insulators: band gaps and quasiparticle energies. *Phys. Rev. B* **34**, 5390–5413 (1986).
32. Autler, S. H. & Townes, C. H. Stark effect in rapidly varying fields. *Phys. Rev.* **100**, 703–722 (1955).
33. Bakos, J. S. AC Stark effect and multiphoton processes in atoms. *Phys. Rep.* **31**, 209–235 (1977).

Acknowledgements

This work was primarily supported by the Center for Computational Study of Excited State Phenomena in Energy Materials, which is funded by the US Department of Energy, Office of Science, Basic Energy Sciences, Materials Sciences and Engineering Division under contract no. DE-AC02-05CH11231, as part of the Computational Materials Sciences Program, which provided the experimental measurements and GW-BSE calculations. The sample fabrication and linear optical spectroscopy was supported by the US Army Research Office under MURI award W911NF-17-1-0312. The pump-probe setup was supported by the ARO MURI award W911NF-15-1-0447. This research used resources of the National Energy Research Scientific Computing Center (NERSC), a DOE Office of Science User Facility supported by the Office of Science of the US Department of Energy under contract no. DE-AC02-05CH11231, and the Extreme Science and Engineering Discovery Environment (XSEDE), which is supported by National Science Foundation grant number ACI-1548562. S.T. acknowledges support from NSF DMR-1552220. K.W. and T.T. acknowledge support from the Elemental Strategy Initiative conducted by the MEXT, Japan and the CREST (JPMJCR15F3), JST. E.C.R. acknowledges support from the Department of Defense (DoD) through the National Defense Science and Engineering Graduate Fellowship (NDSEG) Program. C.-K.Y. and C.S.O. acknowledge useful discussion with A. Srivastava.

Author contributions

C.-K.Y. and F.W. conceived the project. C.-K.Y. supervised the project, designed the experiments and carried out optical measurements, assisted by J.H. and H.D. C.-K.Y. and F.W. analysed the data and performed theoretical analysis, assisted by M.I.B.U. C.-K.Y., M.I.B.U., E.C.R. and A.Z. fabricated the devices. C.S.O., T.C. and S.G.L. performed GW-BSE calculations, Y.S., H.C. and S.T. synthesized MoSe₂ crystals. K.W. and T.T. synthesized hBN crystals. C.-K.Y. and F.W. wrote the manuscript with inputs from all authors.

Competing interests

The authors declare no competing interests.

Additional information

Supplementary information is available for this paper at <https://doi.org/10.1038/s41563-019-0447-8>.

Reprints and permissions information is available at www.nature.com/reprints.

Correspondence and requests for materials should be addressed to C.-K.Y. or F.W.

Publisher's note: Springer Nature remains neutral with regard to jurisdictional claims in published maps and institutional affiliations.

© The Author(s), under exclusive licence to Springer Nature Limited 2019

Methods

Sample fabrication. The MoSe₂ monolayer encapsulated in hBN flakes was prepared with a polyethylene terephthalate (PET) stamp by a dry-transfer method²⁴. Monolayer MoSe₂ and hBN flakes were first exfoliated onto silicon substrate with a 90 nm oxide layer. We used a PET stamp to pick-up the top hBN flake, monolayer MoSe₂ and bottom hBN flake in sequence with accurate alignment based on an optical microscope. The hBN/MoSe₂/hBN heterostructure was then stamped on a silver substrate coated with a 85 nm alumina layer or on a ZnS substrate. Polymer and samples were heated to 60 °C for the pick-up and 130 °C for the stamping process. Finally, the PET was dissolved in dichloromethane for 12 h at room temperature. The sample temperature was kept at 77 K in a liquid-nitrogen-cooled cryostat equipped with BaF₂ window during optical measurements.

Intraexciton optical Stark spectroscopy. Pump–probe spectroscopy study was based on a regenerative amplifier seed by a mode-locked oscillator (Light Conversion PHAROS). The regenerative amplifier delivered femtosecond pulses at a repetition rate of 150 kHz and a pulse duration of ~250 fs, which were split into two beams. One beam was used to pump an optical parametric amplifier and the

other beam was focused onto a sapphire crystal to generate supercontinuum light (500–1,100 nm) for probe pulses. Femtosecond mid-infrared pump pulses with tunable photon energies were generated via difference frequency mixing of the idler pulses from the optical parametric amplifier and residual of fundamental output (1,026 nm) from regenerative amplifier in a 1-mm-thick silver gallium sulfide (AGS) crystal. The generated mid-infrared pump pulse duration was ~400 fs. The cross-correlation of the pump and probe pulses had a full-width at half-maximum close to ~500 fs. The pump–probe time delay was controlled by a motorized delay stage. The probe light was detected by a high-sensitivity CCD line camera operated at 1,000 Hz. The helicity of pump and probe pulses was independently controlled using Fresnel rhomb and broadband quarter-waveplates, respectively. The experiment followed a reflection configuration with a normal incidence and collinear pump–probe geometry, where the absorption spectra were extracted from the reflectance contrast as described in the Supplementary information.

Data availability

The data that support the plots within this paper and other findings of this study are available from the corresponding author upon reasonable request.